

UC Berkeley

UC Berkeley Previously Published Works

Title

Regional and correlative sweat analysis using high-throughput microfluidic sensing patches toward decoding sweat.

Permalink

<https://escholarship.org/uc/item/42m195n7>

Journal

Science advances, 5(8)

ISSN

2375-2548

Authors

Nyein, Hnin Yin Yin
Bariya, Mallika
Kivimäki, Liisa
et al.

Publication Date

2019-08-01

DOI

10.1126/sciadv.aaw9906

Peer reviewed

ENGINEERING

Regional and correlative sweat analysis using high-throughput microfluidic sensing patches toward decoding sweat

Hnin Yin Yin Nyein^{1,2,3*}, Mallika Bariya^{1,2,3*}, Liisa Kivimäki⁴, Sanna Uusitalo⁴, Tiffany Sun Liaw¹, Elina Jansson⁴, Christine Heera Ahn¹, John A. Hangasky⁵, Jiangqi Zhao^{1,3}, Yuanjing Lin^{1,3}, Tuomas Happonen⁴, Minghan Chao¹, Christina Liedert⁴, Yingbo Zhao^{1,3}, Li-Chia Tai^{1,2,3}, Jussi Hiltunen⁴, Ali Javey^{1,2,3†}

Copyright © 2019
The Authors, some
rights reserved;
exclusive licensee
American Association
for the Advancement
of Science. No claim to
original U.S. Government
Works. Distributed
under a Creative
Commons Attribution
NonCommercial
License 4.0 (CC BY-NC).

Recent technological advancements in wearable sensors have made it easier to detect sweat components, but our limited understanding of sweat restricts its application. A critical bottleneck for temporal and regional sweat analysis is achieving uniform, high-throughput fabrication of sweat sensor components, including microfluidic chip and sensing electrodes. To overcome this challenge, we introduce microfluidic sensing patches mass fabricated via roll-to-roll (R2R) processes. The patch allows sweat capture within a spiral microfluidic for real-time measurement of sweat parameters including $[\text{Na}^+]$, $[\text{K}^+]$, [glucose], and sweat rate in exercise and chemically induced sweat. The patch is demonstrated for investigating regional sweat composition, predicting whole-body fluid/electrolyte loss during exercise, uncovering relationships between sweat metrics, and tracking glucose dynamics to explore sweat-to-blood correlations in healthy and diabetic individuals. By enabling a comprehensive sweat analysis, the presented device is a crucial tool for advancing sweat testing beyond the research stage for point-of-care medical and athletic applications.

INTRODUCTION

Sweat is an attractive biofluid for point-of-care health monitoring because it can be locally and noninvasively induced and carries diverse biomolecules ranging from small electrolytes and metabolites to hormones and larger proteins that filter in from deeper in the body (1–5). This ease of access and rich composition give sweat potential to be used to probe the state of the body at a chemical level. Sweat testing has historically been used in applications ranging from medical diagnosis of cystic fibrosis and autonomic neuropathy to assessment of fluid and electrolyte balance in endurance athletes (6–10). Traditional methods for sweat testing require off-body measurements in specialized settings by trained experts, preventing individuals from monitoring their health status immediately, independently, or routinely (11, 12). By taking advantage of flexible and hybrid electronics (13–17), wearable sweat sensors address this limitation by enabling in situ sweat measurements with real-time feedback, creating potential for preventive care, timely diagnosis, and treatment (18–34). Yet, wearable sweat sensor development has stagnated at the experimental and laboratory stage, largely due to an incomplete understanding of sweat dynamics and the physiological information carried in sweat. Sweat behaviors of only a few analytes, including ethanol and chloride, have been extensively investigated and related to blood concentrations or health status (6, 8, 27, 35). Preliminary or small-scale correlation studies have shown

promising applications for other analytes such as metabolites and certain neuroimmune biomarkers present in sweat (3, 27–29, 36), including a recent work that shows how exercise sweat glucose of three healthy subjects roughly tracks their blood glucose, making a preliminary case for semiquantitative glucose prediction (29). However, more comprehensive studies are needed to robustly establish the diagnostic utility and limitations of sweat testing in these cases. One of the primary obstacles to conducting the large-scale population studies needed to decode sweat is achieving high-throughput fabrication of sweat sensors with uniform, reliable performance and high yield. This is critical to ensuring that sensors can be deployed with minimal preparatory overhead and produced in large enough quantities to support simultaneous regional sweat measurements in multisubject and longitudinal trials.

Roll-to-roll (R2R) rotary screen printing is a promising method for high-throughput and cost-effective fabrication of flexible electronics (37, 38). Laser ablation allows for rapid materials patterning at small scales and is useful for engraving microfluidic channels into flexible plastic substrates (39, 40). These R2R-compatible methods are advantageous over traditional, multistep lithography and etching processes as components can be mass produced on large substrate areas at high speeds using automated systems with minimal human involvement (41). By uniting R2R rotary screen printing of sensing electronics with R2R laser cutting of microfluidic channels, we present a wearable patch that can be mass produced at high yield for simultaneous sweat flow control and electrical/electrochemical sensing. While R2R printing of electrochemical electrodes and microfluidic structures has been previously and independently introduced, the system presented here further demonstrates R2R fabrication of integrated sweat rate sensors and microfluidics, representing a key application-oriented technological advancement that can help decode the rate-dependent modulation of sweat analyte secretion (41, 42). The patch has two aligned layers: The first hosts a patterned electrode system

¹Department of Electrical Engineering and Computer Sciences, University of California, Berkeley, Berkeley, CA 94720, USA. ²Berkeley Sensor and Actuator Center, University of California, Berkeley, Berkeley, CA 94720, USA. ³Materials Sciences Division, Lawrence Berkeley National Laboratory, Berkeley, Berkeley, CA 94720, USA. ⁴VTT-Technical Research Centre of Finland, Kaitoväylä 1, FIN-90590 Oulu, Finland. ⁵California Institute for Quantitative Biosciences (QB3), University of California, Berkeley, Berkeley, CA 94720, USA.

*These authors contributed equally to this work.

†Corresponding author. Email: ajavey@berkeley.edu

for transducing analyte concentrations and monitoring sweat rate, and the second is a microfluidic adhesive layer with a sweat collection reservoir and a spiral microfluidic channel to guide sweat flow. Encapsulating sweat within the microfluidic facilitates accurate sweat analysis by minimizing evaporation and environmental contamination and providing efficient sweat sampling to reduce mixing and carryover effects. The wearable patch can monitor sweat parameters such as $[\text{Na}^+]$, $[\text{K}^+]$, [glucose], and sweat rate simultaneously at diverse regions of the body. We specifically demonstrate its use for applications in exercise physiology and medical health monitoring. Localized sweat behavior is extrapolated to estimate whole-body fluid and electrolyte loss toward dehydration monitoring during exercise. Regional iontophoresis sweat parameters are investigated toward decoding sweat for medical diagnostics, including studying electrolyte relations and the correlation between sweat and blood glucose levels for healthy and diabetic subjects. Through its rapid manufacturability and by enabling diverse analysis of sweat dynamics and composition, the presented device bridges a key gap in our ability to decode sweat toward personalized, point-of-care health and fitness monitoring.

RESULTS AND DISCUSSION

High-throughput R2R fabricated microfluidic sensing patches

The wearable sweat patch is assembled by combining a printed sensing layer, microfluidic adhesive spacer, and flexible cover sheet. The sensing layer is fabricated using R2R rotary screen printing, as illustrated in Fig. 1A. The sensing layer, shown in fig. S1, hosts conductive silver base electrodes with active areas modified by a chemically inert graphite-based ink to support electrochemical sensing. Two parallel, spiraling silver lines are patterned alongside for impedimetric sweat rate measurement, while double dielectric polymer layers are printed in-between to insulate the electrode paths and prevent short circuiting between the electrochemical and impedimetric systems. Overall, this layer-by-layer printed sensing architecture allows versatile designs including spiral and serpentine patterns, exhibited in Fig. 1B, that are printed together on a 100-m web length at a rate of 60 devices per minute. The microfluidic adhesive layer and cover sheet are laser cut to define and encapsulate channels for sweat flow. By simply laminating the double-sided microfluidic adhesive between the cover sheet and sensing layer as illustrated in Fig. 1C, tight sealing of the microfluidic channel is achieved. In this way, the device layers can be printed and assembled rapidly and uniformly.

The assembled patch shown in Fig. 1D allows simultaneous electrochemical measurement of sweat analytes and electrical measurement of sweat rate by using electrodes deliberately positioned within a sweat collection reservoir and microfluidic channel. As sweat secretion begins, sweat first accumulates in the collection reservoir at the microfluidic entry point until reaching the chamber's capacity of approximately 2.5 μL . As sweating continues, sweat gland secretory pressure and capillary action push older, accumulated sweat from the collection reservoir into the spiraling microfluidic channel. Electrochemical sensors located within the collection reservoir measure analyte concentrations in newly secreted sweat, minimizing mixing and carryover effects that could otherwise limit the accuracy of continuous measurement. The two spiral silver electrodes, aligned and embedded in the microfluidic channel, are progressively more

immersed in fluid as sweat travels within the channel, resulting in a reduced impedance between them that can be calibrated into continuous, real-time sweat rate measurements. With its simultaneous analyte and sweat rate measurement capabilities, high-throughput manufacturability, and simple assembly, the presented patch enables diverse population studies to uncover relationships between sweat parameters and health or fitness status. As a first step toward decoding sweat, we conduct a number of these studies as summarized in Fig. 1E. These include using the sweat patch to probe regional and temporal sweat behaviors and their application toward predicting whole-body fluid/electrolyte loss during exercise. We further analyze chemically induced, iontophoretic sweat components including the sweat glucose levels of healthy and diabetic subjects (Fig. 1E). The results of these studies will be presented further on in this work.

Characterization of functionalized patches

To confirm that the sensing patch can support high-performing electrochemical sensors, we functionalize the sensing electrodes into Na^+ , K^+ , and glucose sensors and calibrate each in standard solutions that cover the typical sweat concentration range of each analyte (23). Figure 2A shows the general performance of a Na^+ sensor in 15 to 120 mM NaCl solutions. The sensor remains stable throughout the measurement period with a sensitivity of 56.2 mV/decade, similar to sensitivities achieved by lithography-based Na^+ sensors and close to the Nernstian ideal (23). Similarly, the K^+ sensor shows a sensitivity of 51.3 mV/decade in standard solution of 5 to 40 mM KCl (Fig. 2B). The enzymatic glucose sensor has a sensitivity of 1.0 nA/ μM with a linear response over the tested concentration range of 50 to 200 μM (Fig. 2C). Here, the transient portion (shown in fig. S2) of the chronoamperometry curve is removed. To explore the performance uniformity across similarly functionalized patches, 30 Na^+ sensors are fabricated and calibrated in standard NaCl solutions. The sensors show a consistent response to concentration changes as demonstrated by nearly parallel, linear calibration curves in Fig. 2E. The vertical distribution in the calibration curves indicates that sensors vary in their absolute potential at each measured concentration. Specifically, the potential distribution in 60 mM NaCl solution is presented in Fig. 2F and shows that the sensor signal varies between 280 and 317 mV for the 30 tested patches. In contrast, the distribution in sensitivities is tightly bound around an average of 55.7 mV/decade with an SD of 1.1 mV/decade, as shown by the histogram in Fig. 2G. Similarly, as illustrated in fig. S2, glucose sensors are highly reproducible with SDs of 2.9, 2.7, 2.2, 1.9, 2.2, 3.4, and 7.4 nA for tested concentrations of 0, 25, 50, 100, 200, 300, and 400 μM , respectively. These small deviations indicate that one-point calibration is sufficient to characterize the sensors before use. This is a standard practice for electrochemical sensors as even commercial pH meters require precalibration in standard buffer solutions. Note that the microfluidic channel that is connected to the electrochemical sensors is made mildly hydrophobic using short-term heat treatment before bonding to the electrochemical sensors, so calibration solution will not readily flow into or contaminate the channel.

We next characterize performance of the sweat rate sensing electrodes. This sensor operates by measuring admittance between the parallel spiral Ag electrodes contained in the microfluidic channel. As fluid flows along the channel, admittance between the two electrodes increases due to increasing conductivity, creating a relationship between admittance and encapsulated fluid volume. Here, measurements are operated at 100 kHz such that capacitance

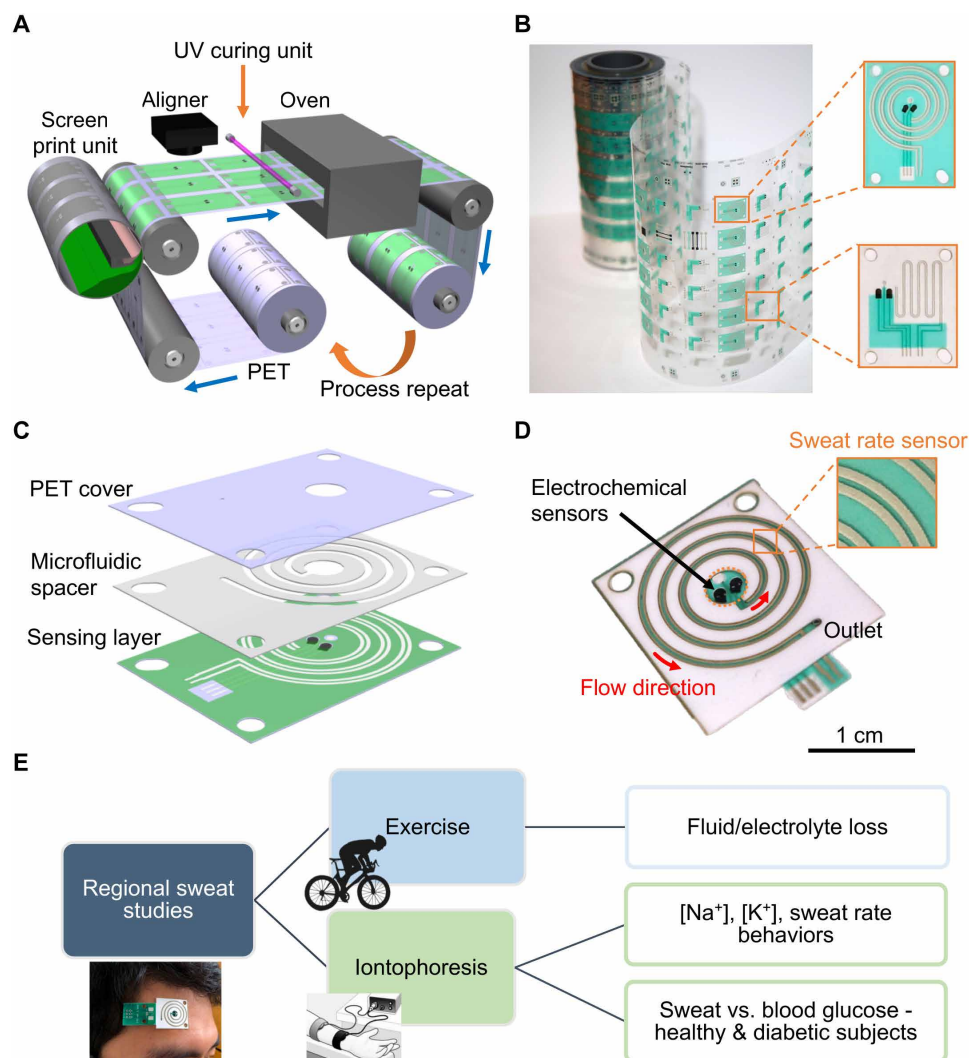


Fig. 1. Schematics of R2R fabricated sweat sensing patches for regional and correlative sweat analysis. (A) R2R rotary screen printing of the wearable biosensing patch and (B) optical image of sensing electrode patterns printed via R2R processing are shown. (C) The biosensing patch is assembled by combining the sensing layer, microfluidic adhesive spacer, and PET cover sheet. (D) The assembled biosensing patch includes electrochemical sensors contained within the collection reservoir and electrical sweat rate sensor embedded in the microfluidic channel. (E) The patch, connected to printed circuit board (PCB), can be worn at various parts of the body for regional studies of the composition and dynamics of exercise and iontophoretic sweat. Photo credit: Antti Veijola (VTT) and Hnin Yin Yin Nyein (University of California, Berkeley).

effects are minimized, allowing admittance to be dominated by a resistance component that produces a simple relation with fluid volume. Figure 2D shows this relationship for test solution containing 15 to 120 mM NaCl concentration, roughly modeling sweat since Na⁺ and Cl⁻ are its primary ionic constituents and dominate its conductivity. Since admittance is a dual function of ionic conductivity and the volume contained in the channel, it is possible to compute the volume based on the conductivity and the admittance for real-time sweat analysis. Having a Na⁺ sensor at the inlet allows determination of ionic conductivity of sweat, and this information is used to look for the admittance and convert to volume contained inside the channel for on-body sweat analysis discussed in the later sections. To measure reproducibility across the spiral electrodes, resistance of five electrodes per each rotation of the printing cylinder for 179 such rotations (895 electrodes in total) are measured to have a relative SD of 2.9%.

Further, 30 sweat rate sensors are studied for performance variation in 60 mM NaCl solution, as displayed in Fig. 2H. Similar to the Na⁺ sensor, the sweat rate sensor has variation in measured admittance at a fixed fluid volume but with comparable behavior across all sensors. Hence, performing sensor calibration with standard NaCl solutions before use allows for accurate sweat rate monitoring for experimental purposes. However, for the general users, it is not necessary as the sensitivity is relatively uniform across sensors. Hence, measurement inaccuracy will be present at the first measurement point but not as substantially in the subsequent ones since the change in admittance is a critical factor to convert to sweat rate.

Regional sweat analyses for predicting whole-body fluid loss
Maintaining fluid/electrolyte balance is essential for healthy vital functions. This is especially relevant in athletics, where proper fluid

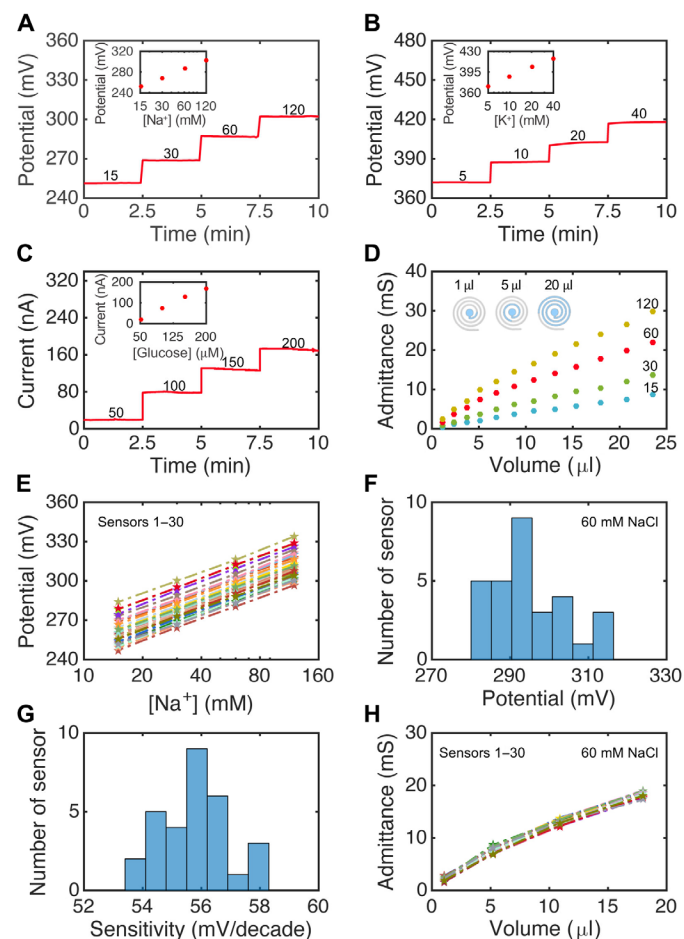


Fig. 2. Characterization of the sweat patch sensors. General performance of (A) Na^+ , (B) K^+ , and (C) glucose sensors functionalized on printed Ag/C electrodes is shown. Measurements are paused when testing solution is changed to a new concentration, and only the last 2.5 min of data is displayed [transient portion in (C), as represented in fig. S2, is removed]. (D) Relationship between fluid volume contained in the microfluidic channel and admittance measured across the Ag sweat rate electrodes in 15 to 120 mM NaCl solutions is shown. (E) Calibration curves of 30 Na^+ sensors in 60 mM NaCl solution, (F) histogram showing variation in the open-circuit potential of 30 Na^+ sensors in 60 mM NaCl solution, (G) sensitivity variation of the 30 sensors, and (H) performance variation across 30 sweat rate sensors in 60 mM NaCl solution are presented.

replacement during practice and competition is critical for ensuring physical and mental well-being (43, 44). As sweating correlates with whole-body fluid loss and is the primary source of electrolyte excretion during exercise, sweat testing can be used to monitor fluid/electrolyte imbalances (11, 45). To understand the relation between local sweat parameters and whole-body losses, we use the wearable sweat patch to first study regional variations in sweat composition and rate. Forehead, ventral forearm, underarm, and upper back regions are monitored as shown in Fig. 3A. Figure 3 (B to D) shows the real-time sweat $[\text{Na}^+]$ and secretion rate of subjects 1 to 3, and Fig. 3 (E to G) is obtained based on Fig. 3 (B to D) to correlate sweat $[\text{Na}^+]$ and secretion rate at various points in time. More specifically, Fig. 3 (B to D) shows simultaneous, continuous measurement of sweat $[\text{Na}^+]$ and sweat rate for three subjects performing stationary biking. The measurements are conducted for up to 30 min or until the

microfluidic channel is fully filled. Subject 3 did not visibly sweat on the forearm, so no data were collected from this region. All subjects showed slightly different but consistent $[\text{Na}^+]$ levels across the four areas. Specifically, subject 1 has higher $[\text{Na}^+]$ in all regions than subject 3, whose $[\text{Na}^+]$ is, in turn, higher than subject 2. Across subjects, the forearm has slightly lower $[\text{Na}^+]$ than other parts of the body, a finding that is supported by previous physiology studies (45). Sweating begins earliest and has the fastest secretion rate at the forehead, while it begins latest and occurs slowest at the forearm. This finding is consistent with earlier reports indicating that the forehead can have up to seven times higher sweat rate than other body regions (45). This makes the forehead a suitable candidate for whole-body fluid loss estimation. Note that despite subjects 1 and 2 having similar sweat rates, their $[\text{Na}^+]$ differ significantly. To explore how sweat sodium composition relates to sweat rate, we explore the relation between sweat $[\text{Na}^+]$ and sweat rate across body regions obtained in Fig. 3 (B to D). Figure 3 (E to G) shows that sweat $[\text{Na}^+]$ and secretion rate are typically positively correlated, but the individual relations cannot be generalized between regions and subjects. A more detailed off-body analysis is conducted on a single subject, as displayed in fig. S3, and verifies the trend that Na^+ excretion generally becomes faster with increasing sweat rate. These findings agree with previous investigations of exercise sweat (21, 46, 47).

We next consider how regional sweat monitoring can be used to estimate whole-body fluid and electrolyte loss. Figure 3H displays the relation between regional sweat rate and whole-body fluid loss rate for subject 1 across four locations. The forehead and forearm have the strongest correlation with Pearson's correlation coefficient (r) of 0.70 and 0.68 and P values of 0.012 and 0.014 for the forehead and forearm, respectively. Correlation plots for two additional subjects are presented in fig. S4. If regional sweat rate versus whole-body fluid loss rate is accumulated across all subjects, then a general positive correlation can be obtained but is not as well defined as when individuals are considered separately, an observation supported by exercise physiology studies (45). Therefore, regional-to-whole-body fluid loss relations are best constructed for each individual and tailored into a personalized algorithm for fluid loss estimation. For example, in Fig. 3I, whole-body fluid loss of subject 1 is predicted from regional sweat loss at the forehead and forearm using the relationship obtained in Fig. 3H. Measured and predicted whole-body fluid losses are close to 1:1. Real-time prediction is additionally performed in Fig. 3J to demonstrate how the sweat patch can be worn as a smart headband or wristband for continuous monitoring of fluid loss. Similarly, whole-body electrolyte loss can also be estimated from regional sweat patterns. Figure S5 shows the total Na^+ secretion rate predicted from measured forearm $[\text{Na}^+]$ and whole-body sweat rate. These experimental results indicate that local sweat parameters can be continuously monitored in situ to notify individuals of their hydration status and electrolyte balance. In the future, a simple resistive temperature sensor could also be printed in the sensing patch so that skin/sweat temperature can be monitored in parallel with sweat composition. This temperature sensor can be used to compensate for environmental temperature influences on the electrochemical sensors (23).

Iontophoretic sweat relations

While understanding the composition of exercise sweat is important for athletic and physiology applications, chemically induced sweat is more useful for medical diagnostics in sedentary conditions (27).

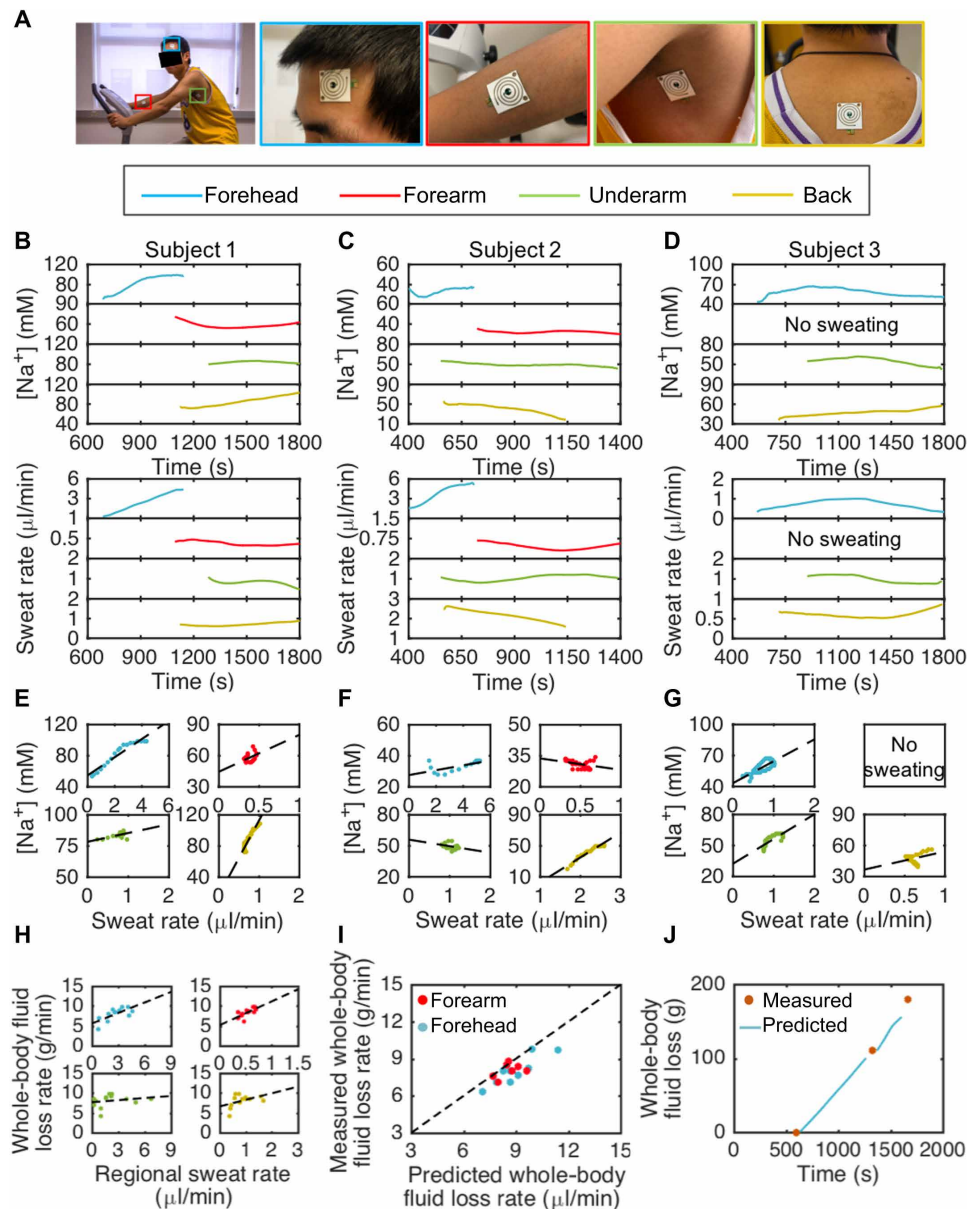


Fig. 3. Regional analysis of exercise sweat during stationary cycling. (A) Biosensing patches are worn on the subject's forehead, forearm, underarm, and back, and sweat parameters in these locations are monitored simultaneously. PCB is not attached to the sweat patch in the images. Multiplexed, regional exercise sweat measurements of $[Na^+]$ and secretion rate for subjects 1, 2, and 3 are displayed in (B), (C), and (D). Relationship between measured sweat $[Na^+]$ and sweat rate for subjects 1, 2, and 3 are plotted in (E), (F), and (G). (H) Relationships between whole-body fluid loss rate and regional sweat rate of subject 1 show strong positive relations on forehead and forearm. (I) Measured and predicted whole-body fluid loss rate of subject 1 at discrete times are close to 1:1. (J) Real-time prediction of whole-body fluid loss from regional forehead sweat rate is displayed. Predictions are made using the relationships obtained in (I). Photo credit: Bizen Maskey, Suncheon National University.

For this reason, we further study sweat induced through pilocarpine iontophoresis. Figure 4 explores electrolyte trends in iontophoretic sweat obtained from two locations, the forearm and lower leg. Figure 4 (B to D) shows real-time simultaneous measurement of sweat $[Na^+]$, $[K^+]$, and secretion rate for three subjects. The time delay for onset of sweating, which is typically within 3 min after the completion of iontophoresis, is adjusted to zero for display purposes. All three subjects show slightly higher $[Na^+]$ levels for their arm compared to their leg, with comparable sweat rates in both locations. Here, subject 1 in Figs. 3E and 4E is the same subject. However, the

forearm sweat $[Na^+]$ shows very different behavior in exercise and iontophoresis sweat as stimulation mechanism for sweat secretion differs. In addition, sweat $[Na^+]$ is easily influenced by factors such as sweat secretion rate and hydration status. We also observed considerable amount of variations in sweat concentration and secretion rate on single individual from day to day. All these factors can have possible contributions on observed difference in $[Na^+]$. Figure 4 (E to G) explores the relationship between these parameters in more detail based on data obtained in Fig. 4 (B to D). While subjects 2 and 3 have $[Na^+]$ and $[K^+]$ increasing with sweat rate, subject 1 consistently

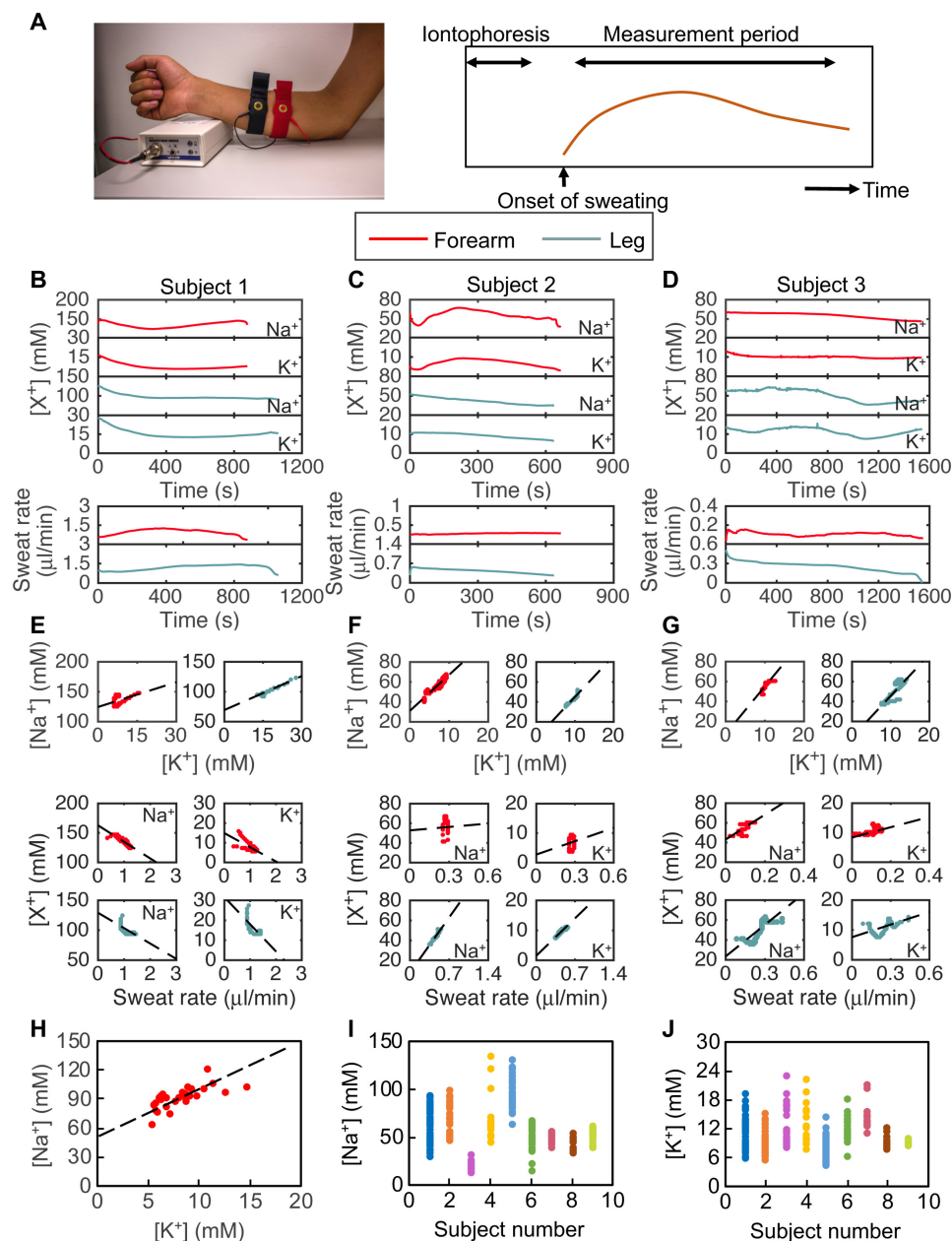


Fig. 4. Regional analysis of iontophoretic sweat electrolytes and secretion rate. (A) Schematics showing iontophoretic sweat extraction and regional analysis of iontophoretic sweat electrolytes and sweat rate. Sensors are worn on the forearm and leg to measure dynamic $[\text{Na}^+]$, $[\text{K}^+]$, and sweat rate profiles of three subjects in (B), (C), and (D). Comparison of electrolyte concentrations and sweat rate show strong positive correlation for two of the three subjects, while $[\text{Na}^+]$ correlates strongly with $[\text{K}^+]$ for all subjects in (E to G). (H) Off-body analysis of collected iontophoresis sweat samples corroborates the strong relation between $[\text{Na}^+]$ and $[\text{K}^+]$. (I) Comparison of $[\text{Na}^+]$ ranges of multiple subjects and (J) $[\text{K}^+]$ ranges of those subjects show that subjects with higher sodium levels often have lower potassium levels when comparing across the population. Photo credit: Bizen Maskey, Suncheon National University.

shows the opposite trend. For all subjects, $[\text{Na}^+]$ and $[\text{K}^+]$ levels are positively correlated. This is corroborated by data from sweat samples collected and tested off-body using a commercial inductively coupled plasma mass spectrometry (ICP-MS) tool, as shown in Fig. 4H, for one subject whose $[\text{Na}^+]$ and $[\text{K}^+]$ levels have a Pearson's correlation coefficient of 0.70. Similar strong correlations are found for other subjects in fig. S6. Over the course of several iontophoresis trials, it is possible to build the range of $[\text{Na}^+]$ and $[\text{K}^+]$ in the sweat of each subject. Comparing these ranges across individuals in Fig. 4 (I and J), subjects

with relatively higher $[\text{Na}^+]$ tend to have lower $[\text{K}^+]$. As both Na^+ and K^+ in sweat share Cl^- as their primary counter ion, a balance between the cation levels is consistent with the fluid's overall charge neutrality (21).

Sweat-to-blood glucose correlations for healthy and diabetic subjects

Another important component of iontophoresis sweat is glucose. There is widespread interest in using sweat glucose as a noninvasive alternative to fingerstick blood glucose measurements for diabetes

monitoring and management (27, 48, 49). While glucose has been studied in exercise and thermal sweat (28, 29), iontophoretic sweat is particularly attractive for this application as on-demand, local sweat secretion would be the most convenient choice for a discreetly worn medical device. However, there has been insufficient analysis of iontophoretic sweat glucose dynamics and sweat-to-blood glucose correlations to verify whether sweat-based diabetes management is feasible. Looking at basal sweat and blood glucose changes is important for establishing whether sweat can be used to diagnose prediabetes or diabetes and for detecting the onset of glucose events such as hypoglycemia so that they may be prevented through medication. Because of technology limitations, previous works have often been unable to consider basal changes in sweat glucose as delays and averaging are introduced while collecting enough sweat for off-body measurement (48). The sweat patch presented here enables immediate and sensitive sweat glucose measurements that allow for refined, basal sweat-to-blood glucose correlations to be investigated.

Toward this goal, we measure real-time glucose dynamics in the iontophoretic sweat of healthy and diabetic subjects as shown in Fig. 5 (A and B, respectively). A new sensor patch is used per trial as the glucose sensors initially have similar currents and sensitivities within the batch but vary in their performance after undergoing wetting and drying that mechanically strains the sensing membranes. Two trials are conducted for each subject to observe longitudinal variations in how sweat glucose and sweat rate react to blood glucose changes. The glucose sensor response time is about a minute after sweat coverage of the sensor surface. This occurs within a couple of minutes of the onset of sweating. Thirty minutes of measurements were performed. In the healthy subject's first trial, sweat glucose decreases from 80 to 72 μM over the 12-min sweating period, while blood glucose decreases from 85 to 79 mg/dl. In the second trial, although the higher average sweat glucose parallels the higher blood glucose level, over the measurement period, the sweat glucose concentration increases from 112 to 122 μM , while the blood glucose level falls by 16 mg/dl. Sweat rate reduces relatively sooner in the first trial compared to the second. For the diabetic subject, sweat rate is relatively stable across both trials, and sweat glucose evolves in the same direction as blood glucose in both trials. In the first trial, sweat glucose increases from 40 to 74 μM as blood glucose increases by 10 mg/dl, while in the second trial, sweat glucose decreases from 35 to 20 μM as blood glucose falls by only 1 mg/dl. The degree of change in sweat glucose concentration does not consistently track how much the blood glucose level has evolved. To verify this finding, we conduct off-body measurements of sweat glucose over multiple trials for a single healthy subject, as shown in Fig. 5C. The glucose profiles over approximately 30 min of sweat collection and measurement per trial show a rapid decrease in concentration followed by a gradual increase for this subject, indicating a complex glucose secretion dynamic that does not consistently follow the change in blood glucose. The glucose profiles for this subject differ from those of the subjects in Fig. 5 (A and B), which could be due to variation in the sweat rate profiles, with higher sweat rates diluting the secreted glucose concentrations for certain subjects, or due to more complex inter-subject variations. Further, the average sweat glucose level for each trial does not correlate one to one with average blood glucose: While average sweat [glucose] is 68, 78, 90, and 95 μM for the four trials, average blood glucose is 83, 83, 122, and 113 mg/dl, respectively. In this study, time lag is not considered as we expect equilibrium between sweat and blood and as the blood glucose levels remain

relatively stable during fasting. Confirmation of the sweat glucose sensor accuracy, and verification of the sweat glucose concentrations and trends, is conducted via comparison to liquid chromatography (LC) in figs. S7 and S8. Further, all measured blood glucose values corresponding to the average values mentioned here are included in table S2.

To investigate sweat-to-blood glucose relations more comprehensively, we conduct a population study of fasting blood and sweat glucose levels across healthy and diabetic cohorts of 20 and 28 subjects each. As fasting blood glucose can be indicative of diabetic state—with universal thresholds for healthy, prediabetic, and diabetic diagnoses—it is important to determine whether fasting sweat levels consistently and universally correlate with blood (50). Figure 5D shows the result of comparing average sweat glucose concentration with blood glucose across all subjects. All the data considered together give a mild positive correlation with a Pearson correlation coefficient of 0.3 and a *P* value of 0.016. Considering the healthy and diabetic cohorts independently and removing an outlying point in both sets that is beyond 2 SDs of the mean, we obtain correlation coefficients of 0.28 and 0.42 with *P* values of 0.167 and 0.016, respectively, indicating weak positive correlations in these sets with poor statistical significance. Overall, there is significant spread in the data, indicating that iontophoretic sweat glucose concentration does not robustly predict blood levels. However, sweat glucose concentration is expected to be sweat rate dependent—for example, one possible model suggests that glucose flux (the amount of glucose secreted through a sweat gland per time) is largely independent of sweat rate, meaning that glucose concentrations are diluted at higher sweat rates (51). Taking this model into account, we consider how the glucose secretion rate relates to blood glucose by multiplying each subject's average sweat glucose concentration and sweat rate, as shown in Fig. 5E. The result is a poorer correlation with a Pearson coefficient of 0.2. Given that a simple relation does not seem to exist across healthy and diabetic cohorts, obtaining longitudinal data for single subjects is one of the next steps to more deeply explore the glucose relation between sweat and blood. Understanding the mechanism of sweat glucose secretion could lend a physiological basis for more sophisticated models that account for or normalize by sweat rate, which may produce a stronger relationship with blood glucose. Stronger correlations may also be found by considering intrasubject correlations between sweat glucose flux and sweat rate. This remains an avenue of future work that could identify regimes in which sweat glucose matches blood concentrations. Overall, these results indicate that it would be difficult to accurately predict instantaneous blood glucose levels by considering iontophoresis sweat glucose and sweat rate alone with simple models. This does not preclude the possibility of a more complex relation existing between sweat components and blood glucose, including multiparameter dependencies and lag times. Further, while the lack of a uniform sweat-to-blood glucose correlation across all subjects makes it difficult to identify universal sweat thresholds for diabetes diagnostics or management, it is possible that more thorough longitudinal studies of sweat glucose could give rise to individual-specific relations between sweat and blood for personalized diabetes management.

Last, to decode sweat glucose more holistically, it would be further insightful to compare glucose variations across body sites, for exercise sweat, and in response to glucose intake. Because the body undergoes dynamic physiological changes during the exertions of exercise, whereas local sweat stimulation via iontophoresis leaves the overall body largely

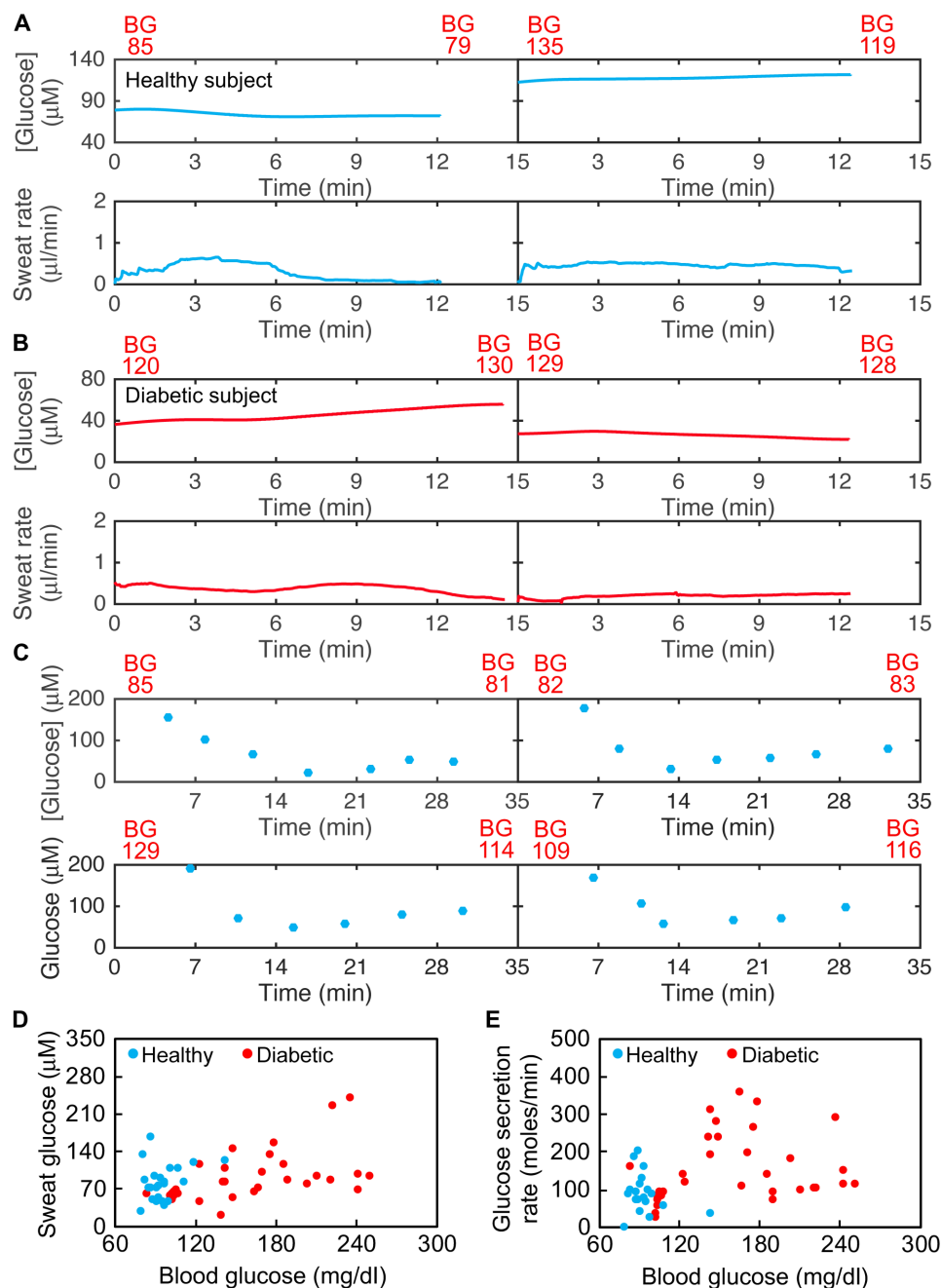


Fig. 5. Regional analysis of iontophoretic sweat glucose and secretion rate in healthy and diabetic subjects. Real-time measurements of iontophoretic sweat [glucose] and sweat rate for (A) one healthy and (B) one diabetic subject repeated in two trials each show variation in sweat glucose response to changing blood glucose levels. (C) Off-body measurements of dynamic glucose profiles in the iontophoretic sweat of one subject across four trials show that sweat glucose levels do not consistently evolve with blood glucose. (D) Fasting levels of average sweat glucose versus blood glucose of 20 healthy and 28 diabetic subjects. (E) Average sweat glucose secretion rate versus blood glucose across the healthy and diabetic cohorts.

in its resting state, the resulting sweat compositions may differ. For example, exercise sweat glucose may be more diluted due to the higher sweat secretion rates and show a decrease with time as glucose is rapidly flushed out of the sweat gland (23). Further work should also characterize continuous sweat glucose dynamic response to large fluctuations in blood glucose, such as over the course of glucose consumption. To better study these and other variables that affect sweat glucose, future studies should explore sweat glucose trends across subjects, intrasubject regional

variation in sweat glucose concentration, and the effect of sweat rate and sweat stimulation times on exercise and iontophoresis sweat glucose.

CONCLUSION

In conclusion, we demonstrate high-throughput fabrication of a wearable microfluidic patch and use it to study sweat composition and correlations at different body locations for exercise and iontophoretic

sweat. R2R printing and laser cutting allow uniform, large-scale fabrication of sensing electrodes and microfluidics that can be rapidly assembled into an integrated device for sweat capture and multiplexed biomarker analysis. Using this patch, we compare sweat secretion rate and sodium levels across body regions during exercise and find that there is typically a positive relation between the two parameters across regions and subjects. We also find a strong relation between local and whole-body fluid loss, making sweat patches a convenient tool for tracking hydration status. In iontophoretic sweat, we monitor sweat electrolytes and sweat rate and find that, while sweat $[\text{Na}^+]$ and $[\text{K}^+]$ are generally positively correlated for any one individual, subjects with higher sodium levels often have lower potassium levels when comparing across a population. We further study the relation between iontophoretic sweat glucose and blood glucose for healthy and diabetic subjects. We find that an individual's blood glucose changes are not matched by consistent sweat glucose changes and that fasting sweat glucose levels do not strongly correlate with fasting blood glucose levels across a population of healthy and diabetic subjects. While this finding limits the establishment of universal, sweat glucose-based thresholds for diabetes diagnostics, it does not bar the possibility of more complex, individual-specific correlations existing between sweat and blood glucose.

Moving forward, further improvements to fabrication throughput of the sweat patch will be achieved via direct R2R dispensing of functional materials onto the printed electrodes, reducing sensor performance variations that arise from manual drop-casting of sensing layers. To more holistically decode sweat, the dynamics of other sweat analytes will be targeted in large-scale subject studies that include both healthy and afflicted cohorts. Since sweat composition is modulated by a variety of factors including age, body mass, diet, and hydration status (46), more comprehensive longitudinal studies will be conducted to extract personalized relations between sweat parameters and medical or physiological status. By helping to interpret the rich chemical information contained in sweat, these studies will ultimately determine the uses and limitations of sweat sensing going forward.

MATERIALS AND METHODS

Materials

Sodium ionophore X, bis(2-ethylhexyl) sebacate (DOS), high-molecular weight polyvinyl chloride (PVC), sodium tetrakis[3,5-bis(trifluoromethyl)phenyl]borate (Na-TFPB), tetrahydrofuran (THF), polyvinyl butyral resin BUTVAR B-98, valinomycin (potassium ionophore), sodium tetraphenylborate (NaTPB), sodium chloride (NaCl), 3,4-ethylenedioxythiophene (EDOT), and poly(sodium 4-styrenesulfonate) (NaPSS), glucose oxidase GOx (from *Aspergillus niger*), and agarose were purchased from Sigma-Aldrich. Silicone rubber (3140 RTV silicone) was purchased from Ellsworth Adhesives. Thermoplastic polyurethane (TPU) (Tecoflex SG-80A) was purchased from Lubrizol.

Fabrication of microfluidic patches

Polyethylene terephthalate (PET) substrate (125 μm ; Melinex ST506) was run at a speed of 2 m/min through ovens with a length of 4 m and heated to 140°C. R2R printing on the primed PET included printing of (i) underlying silver electrodes, (ii) carbon electrodes, (iii) dielectric polymer layers, and (iv) upper spiral silver electrodes as illustrated in fig. S1. The silver electrode head for electrochemical

sensing is 1 mm in diameter, while the carbon electrode head is 1.5 mm in diameter. The sweat rate sensor's silver electrode lines are 500 μm wide and spaced 300 μm apart. Alignment between printed layers was monitored by a camera module. Silver and carbon layers were cured in ovens, while the dielectric layer was UV cured. Materials and processing parameters used during R2R fabrication are listed in table S1. The microfluidic contains a collection reservoir that is 5 mm in diameter and a channel that is 150 mm long with a cross section of 180 μm by 900 μm to contain a total volume of 24.3 μl . In this work, double-sided adhesive tape (3M 9965) was used as the microfluidic layer. The cover sheet designed to enclose the microfluidic channel was formed from polyester film (3M 9984). After R2R processing, the sensing electrode layer, microfluidic adhesive, and cover sheet were cut by a UV laser. Laser system (ELAS) was equipped with a camera module to align laser beam with the alignment marks. Last, the electrochemical sensors comprising sensing layer, microfluidic layer, and cover lid were manually assembled, as illustrated in Fig. 1C.

Printing of the spiral Ag electrodes onto the thick dielectric layer required modifications to the printing tools and layer design/layout compared to when ink was printed directly onto smooth plastic substrate or over thinner printed layers. To achieve reliable and good ink transfer onto the dielectric layer, coarser screens with higher ink transfer but poorer resolution were used. As a result, the spiral lines have comparatively larger spacing and line widths. Resistance of the lower and upper printed Ag lines was measured by a stop-and-go characterization system with a four-probe measurement unit (PXI-4072, National Instruments).

Functionalization of Na^+ , K^+ , and glucose sensors

Na^+ -selective polymeric solution was produced by mixing 30:10:65:0.55:1 weight ratio of PVC, silicone rubber, DOS, Na-TFPB, and Na ionophore X in 660 μl of THF. K^+ -selective solution was produced by dissolving 47:60:96:1:4 weight ratio of TPU, silicone rubber, DOS, NaTPB, and valinomycin in 700 μl of THF. Na^+ (2 $\mu\text{l}/\text{mm}^2$)– and K^+ (3 $\mu\text{l}/\text{mm}^2$)–selective solutions were drop-casted onto the printed carbon electrodes and left to dry overnight under ambient conditions. To fabricate glucose sensors, carbon electrodes were modified by pulse deposition of Au in 0.1 M HAuCl_4 between 0 and -2 V for 2000 cycles at 50 Hz. Glucose-selective cocktail was prepared by first dissolving 0.5% agarose in deionized (DI) water using magnetic stirring at 120°C. The agarose solution was then mixed with GOx solution [10 mg/ml in phosphate buffered saline (PBS) (pH 7.2)] at 2:1 (v/v) ratio. A Prussian blue mediator layer was deposited onto the electrodes by cyclic voltammetry from 0 to 0.5 V (versus Ag/AgCl) for one cycle at a scan rate of 20 mV/s in a solution containing 2.5 mM FeCl_3 , 100 mM KCl, 2.5 mM $\text{K}_3\text{Fe}(\text{CN})_6$, and 100 mM HCl. Three microliters of the glucose-selective cocktail were drop-casted onto the carbon electrodes and left to dry overnight under ambient conditions.

Characterization of Na^+ , K^+ , glucose, and sweat rate sensors

The Na^+ sweat rate sensor was characterized via open-circuit potential measurements in solutions of 15, 30, 60, and 120 mM NaCl. The sensor was conditioned in 120 mM NaCl for 4 hours before characterization. The K^+ sensor was similarly characterized in solutions of 5, 10, 20, and 40 mM KCl. The glucose sensor was characterized using chronoamperometry in PBS buffer solutions at pH 7.2 containing 50, 100, 150, and 200 μM glucose. Measurements were performed by addition of concentrated glucose solution into the testing solution (PBS buffer as

a solvent) and mixing to achieve desired test concentrations. Measurements were not recorded during a mixing and waiting period of 30 s for stabilization, and the transient portion (as shown in fig. S2) was removed. Impedance-based sweat rate measurements were performed at 100 kHz using 15, 30, 60, and 120 mM NaCl solutions. Between measurements at each concentration, the microfluidic channel was flushed with DI water multiple times and dried with N₂.

Off-body sweat analysis

Subjects were wiped and cleaned with alcohol swap and DI water at area of interest before each sweat collection began. For whole-body and regional sweat analysis, regional sweat was collected by attaching our sweat patches (without impedance-based sweat rate sensor) at locations of interest. Subjects were asked to bike for 6 to 13 min with 4-min break in between for removing sweat patches, cleaning, weighing nude whole-body weight, and reattaching new sweat patches. Whole-body fluid loss rate was estimated from total nude body weight loss at each time interval. Each trial lasts for a maximum of 1.5 hours. For collected sweat patches from each region and time interval, total sweat contained inside each patch was measured. On the basis of the measured volume of sweat and the time interval, regional sweat rate was computed. Collected sweat from each region and time interval were further analyzed by ICP-MS to measure concentrations of Na⁺ and K⁺.

For iontophoresis sweat analysis, regional sweat was collected for a total of 28 to 32 min using our sweat patches. For time-dependent off-body analysis, subjects were wiped and cleaned with alcohol swap and DI water every 3 to 5 min, and new sweat patches were attached. Sweat from each timed sample was collected from each patch for further analysis by ICP-MS, LC, or glucose sensors.

For off-body sweat glucose measurement, 10 μ l of collected sweat was injected onto the sensor surface, and the current response was recorded by benchtop electrochemical measurement instruments. Following measurement in sweat, a large volume of glucose stock solution (~1 ml) was introduced to overwhelm the glucose contribution from the small sweat volume. Small volumes of high-concentration glucose stock solution were successively injected to calibrate each sensor individually and then to back-calculate the glucose concentration indicated by the original current response to sweat.

On-body sweat analysis using the biosensing patch

On-body human trials were carried out at the University of California, Berkeley in compliance with human research protocols [Committee for Protection of Human Subjects (CPHS) 2014-08-6636] and (CPHS 2015-05-7578) approved by the Berkeley Institutional Review Board. Subjects' forehead, underarm, forearm, back, and leg were wiped and cleaned with alcohol swabs and gauze before attachment of the microfluidic patches. Stationary cycling trials were performed using an electronically braked leg cycle ergometer (Kettler E3 Upright Ergometer Exercise Bike). On-body trials were performed at 23°C and 35% relative humidity in a ventilated laboratory setting, and subjects were asked to maintain a biking power of 150 W. For the whole-body fluid loss study, pre- and postexercise bare body mass were measured using A&D weighing scale FG-150KBM FG-K, while regional sweat loss was measured by the volume of sweat accumulated in the microfluidic patches. Regional sweat measurements correspond to an area of 2 cm by 2 cm of studied site. Iontophoresis trials were performed using the ELITech Group Macroduct sweat collection system. Iontophoresis current application was conducted on the forearm and distal leg for 5 min,

and the biosensing patch was attached immediately after. Blood glucose measurements were performed using commercial test kits (FreeStyle Precision Neo blood glucose meter and test strips) before and after sweat collection or on-body sensing. A new sweat patch was used per trial. Sensors in the patch were calibrated after removal from the subject's body, with identical protocol as off-body sensor calibration. For the sweat-to-blood glucose correlation study, subjects performed overnight fasting before their trials. Real-time sweat compositions and secretion rates were recorded using a custom-developed PCB reported earlier by our group in (36). The PCB contains on-site signal conditioning, analysis, and wireless data transmission to a mobile phone for real-time readout of the measured sweat analysis. Sweat rate and composition data obtained during on-body measurements were filtered in MATLAB using the Hampel identifier. Signal outputs from the sensors were averaged every 30 s for correlation study between sweat [Na⁺], [K⁺], and secretion rate in Figs. 3 (E to G) and 4 (E to G).

Sweat glucose measurement using high performance liquid chromatography

Sweat samples were analyzed using high-performance anion exchange chromatography with pulsed amperometric detection (HPAEC) on a Dionex ICS-5000 system (Thermo Fisher Scientific). Samples were injected (10 μ l), and glucose was separated from all other sweat components on a Dionex CarboPAC PA-20 HPAEC column (length, 150 mm; inner diameter, 3 mm; particle size, 6.5 μ m) with an in-line column guard (length, 30 mm; inner diameter, 3 mm; particle size, 6.5 μ m) using an isocratic method (15 min, 0.010 M NaOH). The flow rate was set at 400 μ l/min. The column was cleaned with 0.200 M NaOH (5 min) and reequilibrated in 0.01 M NaOH (15 min) after each run. The column compartment was maintained at 30°C, and the detector compartment was maintained at 25°C. Solvents were prepared using Milli-Q grade ultrapure water (resistivity >18.2 megaohm-cm at 25°C) and NaOH [50% (w/w) NaOH, Certified Grade, Fisher Scientific). A calibration curve was generated from the peak area of glucose standards with known concentrations (5 to 40 μ M). All data were processed using Chromeleon Chromatography Data System software (version 7.1).

SUPPLEMENTARY MATERIALS

Supplementary material for this article is available at <http://advances.sciencemag.org/cgi/content/full/5/8/eaaw9906/DC1>

Computational steps to relate whole-body and regional sweat Na⁺ secretion

Fig. S1. Printing process of the sensing layer includes layering silver base electrodes, conductive graphite ink, dielectric polymer ink, and spiral silver lines.

Fig. S2. Representative glucose sensor chronoamperometry curve with transient portion included and reproducibility of glucose sensors.

Fig. S3. Regional [Na⁺] and sweat rate correlations on the forehead, forearm, underarm, and back of subject 1.

Fig. S4. Whole-body fluid loss rate vs. regional sweat rate correlations.

Fig. S5. Predicted whole-body Na⁺ secretion rate versus measured forearm Na⁺ secretion rate of subject 1.

Fig. S6. Off-body analysis of [Na⁺] and [K⁺] relation in iontophoresis sweat across multiple trials (marked in different colors) for six subjects.

Fig. S7. High-performance liquid chromatography (HPLC) analysis of sweat samples and comparison with sweat sensor response.

Fig. S8. Comparison and correlation of blood glucose measured by blood glucose meter, sweat measured by HPLC, and the sweat glucose sensors.

Table S1. Processing parameters used in R2R printing.

Table S2. Blood glucose measurements for population studies.

REFERENCES AND NOTES

1. B. Schitteck, R. Hipfel, B. Sauer, J. Bauer, H. Kalbacher, S. Stevanovic, M. Schirle, K. Schroeder, N. Blin, F. Meier, G. Rassner, C. Garbe, Dermcidin: A novel human antibiotic peptide secreted by sweat glands. *Nat. Immunol.* **2**, 1133–1137 (2001).

2. S. Robinson, A. H. Robinson, Chemical composition of sweat. *Physiol. Rev.* **34**, 202–220 (1954).
3. G. Cizza, A. H. Marques, F. Eskandari, I. C. Christie, S. Torvik, M. N. Silverman, T. M. Phillips, E. M. Sternberg, POWER Study Group, Elevated neuroimmune biomarkers in sweat patches and plasma of premenopausal women with major depressive disorder in remission: The POWER study. *Biol. Psychiatry* **64**, 907–911 (2008).
4. C. F. Consolazio, R. A. Nelson, L. O. Matoush, R. S. Harding, J. E. Canham, Nitrogen excretion in sweat and its relation to nitrogen balance requirements. *J. Nutr.* **79**, 399–406 (1963).
5. P. J. Derbyshire, H. Barr, F. Davis, S. P. J. Higson, Lactate in human sweat: A critical review of research to the present day. *J. Physiol. Sci.* **62**, 429–440 (2012).
6. L. E. Gibson, R. E. Cooke, A test for concentration of electrolytes in sweat in cystic fibrosis of the pancreas utilizing pilocarpine by iontophoresis. *Pediatrics* **23**, 545–549 (1959).
7. B. M. W. Illigens, C. H. Gibbons, Sweat testing to evaluate autonomic function. *Clin. Auton. Res.* **19**, 79–87 (2009).
8. M. Phillips, M. H. McAloon, A sweat-patch test for alcohol consumption: Evaluation in continuous and episodic drinkers. *Alcohol. Clin. Exp. Res.* **4**, 391–395 (1980).
9. M. F. Bergeron, Heat cramps: Fluid and electrolyte challenges during tennis in the heat. *J. Sci. Med. Sport* **6**, 19–27 (2003).
10. J. T. Korpelainen, K. A. Sotaniemi, V. V. Myllylä, Asymmetric sweating in stroke: A prospective quantitative study of patients with hemispheric brain infarction. *Neurology* **43**, 1211–1214 (1993).
11. L. B. Baker, Sweat testing methodology in the field: Challenges and best practices. *Sports Sci. Exchange* **28**, 1–6 (2016).
12. S. M. Shirreffs, R. J. Maughan, Whole body sweat collection in humans: An improved method with preliminary data on electrolyte content. *J. Appl. Physiol.* **82**, 336–341 (1985).
13. S. Wang, J. Xu, W. Wang, G.-J. N. Wang, R. Rastak, F. Molina-Lopez, J. W. Chung, S. Niu, V. R. Feig, J. Lopez, T. Lei, S.-K. Kwon, Y. Kim, A. M. Foudeh, A. Ehrlich, A. Gasperini, Y. Yun, B. Murmann, J. B.-H. Tok, Z. Bao, Skin electronics from scalable fabrication of an intrinsically stretchable transistor array. *Nature* **555**, 83–88 (2018).
14. H. Fang, K. J. Yu, C. Gloschat, Z. Wang, E. Song, C. H. Chiang, J. Zhao, S. M. Won, S. Xu, M. Trumpis, Y. Zhong, S. W. Han, Y. Xue, D. Xu, S. W. Choi, G. Cauwenberghs, M. Kay, Y. Huang, J. Viventi, I. R. Efimov, J. A. Rogers, Capacitively coupled arrays of multiplexed flexible silicon transistors for long-term cardiac electrophysiology. *Nat. Biomed. Eng.* **1**, 0038 (2017).
15. M. Kaltenbrunner, T. Sekitani, J. Reeder, T. Yokota, K. Kuribara, T. Tokuhara, M. Drack, R. Schwödiauer, I. Graz, S. Bauer-Gogonea, S. Bauer, T. Someya, An ultra-lightweight design for imperceptible plastic electronics. *Nature* **499**, 458–463 (2013).
16. M. C. AlAlpine, H. Ahmad, D. Wang, J. R. Heath, Highly ordered nanowire arrays on plastic substrates for ultrasensitive flexible chemical sensors. *Nat. Mater.* **6**, 379–384 (2007).
17. W. Li, X. Xu, C. Liu, M. C. Tekell, J. Ning, J. Guo, J. Zhang, D. Fan, Ultralight and binder-free all-solid-state flexible supercapacitors for powering wearable strain sensors. *Adv. Funct. Mater.* **27**, 1702738 (2017).
18. J. Choi, R. Ghaffari, L. B. Baker, J. A. Rogers, Skin-interfaced systems for sweat collection and analytics. *Sci. Adv.* **4**, eaar3921 (2018).
19. S. Imani, A. J. Bandodkar, A. M. V. Mohan, R. Kumar, S. Yu, J. Wang, P. P. Mercier, A wearable chemical–electrophysiological hybrid biosensing system for real-time health and fitness monitoring. *Nat. Commun.* **7**, 11650 (2016).
20. M. McCaul, T. Gelnnon, D. Diamond, Challenges and opportunities in wearable technology for biochemical analysis in sweat. *Curr. Opin. Electrochem.* **3**, 46–50 (2017).
21. Z. Sonner, E. Wilder, J. Heikenfeld, G. Kasting, F. Beyette, D. Swaile, F. Sherman, J. Joyce, J. Hagen, N. Kelley-Loughnane, R. Naik, The microfluidics of the eccrine sweat gland, including biomarker partitioning, transport, and biosensing implications. *Biomicrofluidics* **9**, 031301 (2015).
22. N. De Giovanni, N. Fucci, The current status of sweat testing for drugs of abuse: A review. *Curr. Med. Chem.* **20**, 545–561 (2013).
23. W. Gao, S. Emaminejad, H. Y. Y. Nyein, S. Challa, K. Chen, A. Peck, H. M. Fahad, H. Ota, H. Shiraki, D. Kiriya, D.-H. Lien, G. A. Brooks, R. W. Davis, A. Javey, Fully integrated wearable sensor arrays for multiplexed in situ perspiration analysis. *Nature* **529**, 509–514 (2016).
24. T. Glennon, C. O’Quigley, M. McCaul, G. M. S. Beirne, G. G. Wallace, F. Stroeescu, N. O’Mahoney, P. White, D. Diamond, ‘SWEATCH’: A wearable platform for harvesting and analysing sweat sodium content. *Electroanalysis* **28**, 1283–1289 (2016).
25. D. Kinnamon, R. Ghanta, K.-C. Lin, S. Muthukumar, S. Prasad, Portable biosensor for monitoring cortisol in low-volume perspired human sweat. *Sci. Rep.* **7**, 13312 (2017).
26. H. J. Lee, T. K. Choi, Y. B. Lee, H. R. Cho, R. Ghaffari, L. Wang, H. J. Choi, T. D. Chung, N. Lu, T. Hyeon, S. H. Choi, D. H. Kim, A graphene-based electrochemical device with thermoresponsive microneedles for diabetes monitoring and therapy. *Nat. Nanotechnol.* **11**, 566–572 (2016).
27. S. Emaminejad, W. Gao, E. Wu, Z. A. Davies, H. Y. Y. Nyein, S. Challa, S. P. Ryan, H. M. Fahad, K. Chen, Z. Shahpar, S. Talebi, C. Milla, A. Javey, R. W. Davis, Autonomous sweat extraction and analysis applied to cystic fibrosis and glucose monitoring using a fully integrated wearable platform. *Proc. Natl. Acad. Sci. U.S.A.* **114**, 4625–4630 (2017).
28. Y. J. Hong, H. Lee, J. Kim, M. Lee, H. J. Choi, T. Hyeon, D.-H. Kim, Multifunctional wearable system that integrates sweat-based sensing and vital-sign monitoring to estimate pre-/post-exercise glucose levels. *Adv. Funct. Mater.* **28**, 1805754 (2018).
29. A. J. Bandodkar, P. Gutruf, J. Choi, K. Lee, Y. Sekine, J. T. Reeder, W. J. Jeang, A. J. Aranyosi, S. P. Lee, J. B. Model, R. Ghaffari, C. J. Su, J. P. Leshock, T. Ray, A. Verrillo, K. Thomas, V. Krishnamurthi, S. Han, J. Kim, S. Krishnan, T. Hang, J. A. Rogers, Battery-free, skin-interfaced microfluidic/electronic systems for simultaneous electrochemical, colorimetric, and volumetric analysis of sweat. *Sci. Adv.* **5**, eaav3294 (2019).
30. S. Nakata, M. Shiomi, Y. Fujita, T. Arie, S. Akita, K. Takei, A wearable pH sensor with high sensitivity based on a flexible charge-coupled device. *Nat. Electron.* **1**, 596–603 (2018).
31. L.-C. Tai, W. Gao, M. Chao, M. Bariya, Q. P. Ngo, Z. Shahpar, H. Y. Y. Nyein, H. Park, J. Sun, Y. Jung, E. Wu, H. M. Fahad, D.-H. Lien, H. Ota, G. Cho, A. Javey, Methylxanthine drug monitoring with wearable sweat sensors. *Adv. Mater.* **30**, 1707442 (2018).
32. J. Kim, I. Jeeran, S. Imani, T. N. Cho, A. Bandodkar, S. Cinti, P. P. Mercier, J. Wang, Noninvasive alcohol monitoring using a wearable tattoo-based iontophoretic-biosensing system. *ACS Sens.* **1**, 1011–1019 (2016).
33. D. P. Rose, M. E. Ratterman, D. K. Griffin, L. Hou, N. Kelley-Loughnane, R. R. Naik, J. A. Hagen, I. Papautsky, J. C. Heikenfeld, Adhesive RFID Sensor Patch for Monitoring of Sweat Electrolytes. *IEEE Trans. Biomed. Eng.* **62**, 1457–1465 (2015).
34. Y. Yang, W. Gao, Wearable and flexible electronics for continuous molecular monitoring. *Chem. Soc. Rev.* **48**, 1465–1491 (2019).
35. A. Hauke, P. Simmers, Y. R. Ojha, B. D. Cameron, R. Ballweg, T. Zhang, N. Twine, M. Brothers, E. Gomez, J. Heikenfeld, Complete validation of a continuous and blood-correlated sweat biosensing device with integrated sweat stimulation. *Lab Chip* **18**, 3750–3759 (2018).
36. H. Y. Y. Nyein, L.-C. Tai, Q. P. Ngo, M. Chao, G. B. Zhang, W. Gao, M. Bariya, J. Bullock, H. Kim, H. M. Fahad, A. Javey, A wearable microfluidic sensing patch for dynamic sweat secretion analysis. *ACS Sens.* **3**, 944–952 (2018).
37. S. Khan, L. Lorenzelli, R. S. Dahiya, Technologies for Printing Sensors and Electronics Over Large Flexible Substrates: A Review. *IEEE Sens. J.* **15**, 3164–3185 (2015).
38. A. E. Ostfeld, I. Deckman, A. M. Gaikwad, C. M. Lochner, A. C. Arias, Screen printed passive components for flexible power electronics. *Sci. Rep.* **5**, 15959 (2015).
39. B. L. Thompson, Y. Ouyang, G. R. Duarte, E. Carrilho, S. T. Krauss, J. P. Landers, Inexpensive, rapid prototyping of microfluidic devices using overhead transparencies and a laser print, cut and laminate fabrication method. *Nat. Protoc.* **10**, 875–886 (2015).
40. D. Patko, Z. Mártonfalvi, B. Kovacs, F. Vonderviszt, M. Kellermayer, R. Horvath, Microfluidic channels laser-cut in thin double-sided tapes: Cost-effective biocompatible fluidics in minutes from design to final integration with optical biochips. *Sens. Actuators B* **196**, 352–356 (2014).
41. M. Bariya, Z. Shahpar, H. Park, J. Sun, Y. Jung, W. Gao, H. Y. Y. Nyein, T. S. Liaw, L.-C. Tai, Q. P. Ngo, M. Chao, Y. Zhao, M. Hettick, G. Cho, A. Javey, Roll-to-roll gravure printed electrochemical sensors for wearable and medical devices. *ACS Nano* **12**, 6978–6987 (2018).
42. J. Hiltunen, C. Liedert, M. Hiltunen, O.-H. Huttunen, J. Hiitola-Keinanen, S. Aikio, M. Harjanne, M. Kurkinen, L. Hakalahti, L. P. Lee, Roll-to-roll fabrication of integrated PDMS–paper microfluidics for nucleic acid amplification. *Lab Chip* **18**, 1552–1559 (2018).
43. M. Shibasaki, T. E. Wilson, C. G. Crandall, Neural control and mechanisms of eccrine sweating during heat stress and exercise. *J. Appl. Physiol.* **100**, 1692–1701 (2006).
44. N. A. S. Taylor, C. A. Machado-Moreira, Regional variations in transepidermal water loss, eccrine sweat gland density, sweat secretion rates and electrolyte composition in resting and exercising humans. *Extrem. Physiol. Med.* **2**, 4 (2013).
45. L. B. Baker, C. T. Ungaro, B. C. Sopeña, R. P. Nuccio, A. J. Reimeir, J. M. Carter, J. R. Stofan, K. A. Barnes, Body map of regional vs. whole body sweating rate and sweat electrolyte concentrations in men and women during moderate exercise-heat stress. *J. Appl. Physiol.* **124**, 1304–1318 (2018).
46. L. B. Baker, Sweating rate and sweat sodium concentration in athletes: A review of methodology and intra/interindividual variability. *Sports Med.* **47**, 111–128 (2017).
47. I. L. Schwartz, J. H. Thaysen, Excretion of sodium and potassium in human sweat. *J. Clin. Invest.* **35**, 114–120 (1956).
48. J. Moyer, D. Wilson, I. Finkelshtein, B. Wong, R. Potts, Correlation between sweat glucose and blood glucose in subjects with diabetes. *Diabetes Technol. Ther.* **14**, 398–402 (2012).
49. J. Y. Kim, A. S. Campbell, J. Wang, Wearable non-invasive epidermal glucose sensors: A review. *Talanta* **177**, 163–170 (2018).
50. World Health Organization, Definition, Diagnosis, and Classification of Diabetes Mellitus and Its Complications: Report of a WHO consultation. Part 1: Diagnosis and Classification of Diabetes Mellitus. Geneva, World Health Org., 1999.
51. A. Jajack, M. Brothers, G. Kasting, J. Heikenfeld, Enhancing glucose flux into sweat by increasing paracellular permeability of the sweat gland. *PLOS ONE* **13**, e0200009 (2018).

Acknowledgments: We acknowledged M. A. Marletta’s laboratory for use of HPLC.

Funding: This work was supported by the NSF Nanomanufacturing Systems for Mobile

Computing and Mobile Energy Technologies (NASCENT), the Berkeley Sensor and Actuator Center (BSAC), and the Bakar fellowship. **Author contributions:** H.Y.Y.N., M.B., and A.J. conceived the idea, designed the project, and analyzed and interpreted the experimental results. H.Y.Y.N. and M.B. performed experiments with assistance from T.S.L., C.H.A., J.Z., Y.L., and L.-C.T. M.C. developed the printed circuit board. J.A.H. and Y.Z. assisted with the HPLC measurements. L.K., S.U., E.J., T.H., C.L., and J.H. performed R2R fabrication of the sweat patches. **Competing interests:** The authors declare that they have no competing interests. **Data and materials availability:** All data needed to evaluate the conclusions in the paper are present in the paper and/or the Supplementary Materials. Additional data related to this paper may be requested from the authors.

Submitted 12 February 2019

Accepted 8 July 2019

Published 16 August 2019

10.1126/sciadv.aaw9906

Citation: H. Y. Y. Nyein, M. Bariya, L. Kivimäki, S. Uusitalo, T. S. Liaw, E. Jansson, C. H. Ahn, J. A. Hangasky, J. Zhao, Y. Lin, T. Happonen, M. Chao, C. Liedert, Y. Zhao, L.-C. Tai, J. Hiltunen, A. Javey, Regional and correlative sweat analysis using high-throughput microfluidic sensing patches toward decoding sweat. *Sci. Adv.* **5**, eaaw9906 (2019).